

PAPER

# Direct probing of imperfection-induced electrical degradation in millimeter-scale graphene on SiO<sub>2</sub> substrates

To cite this article: Rui-Song Ma *et al* 2019 *2D Mater.* **6** 045033

View the [article online](#) for updates and enhancements.



**Going Greener Together....**

Search and buy our Green Production materials at [www.goodfellow.com](http://www.goodfellow.com)

**Goodfellow**  
GREEN PRODUCTION

- Bio-degradable
- Non-toxic
- Bio-based
- Derived from renewable sources

The banner features a green background with a stylized factory and houses on the left, and a hexagonal grid of material samples on the right. The text is in white and yellow, and the Goodfellow logo is in green and white.



## PAPER

Direct probing of imperfection-induced electrical degradation in millimeter-scale graphene on SiO<sub>2</sub> substratesRECEIVED  
5 June 2019REVISED  
14 July 2019ACCEPTED FOR PUBLICATION  
22 July 2019PUBLISHED  
16 August 2019Rui-Song Ma<sup>1,2</sup>, Jiajun Ma<sup>1,2</sup>, Jiahao Yan<sup>1,2</sup>, Liangmei Wu<sup>1,2</sup>, Hongtao Liu<sup>1,2</sup>, Wei Guo<sup>4</sup>, Shuai Wang<sup>4</sup>, Qing Huan<sup>1,2</sup>, Xiao Lin<sup>1,2</sup>, Lihong Bao<sup>1,2,3</sup>, Sokrates T Pantelides<sup>5,2</sup> and Hong-Jun Gao<sup>1,2</sup><sup>1</sup> Institute of Physics, Chinese Academy of Sciences, PO Box 603, Beijing 100190, People's Republic of China<sup>2</sup> University of Chinese Academy of Sciences and CAS Center for Excellence in Topological Quantum Computation, Chinese Academy of Sciences, PO Box 603, Beijing 100190, People's Republic of China<sup>3</sup> Songshan Lake Materials Laboratory, Dongguan, Guangdong 523808, People's Republic of China<sup>4</sup> Key Laboratory of Material Chemistry for Energy Conversion and Storage, Ministry of Education School of Chemistry and Chemical Engineering, Huazhong University of Science and Technology, Wuhan 430074, People's Republic of China<sup>5</sup> Department of Physics and Astronomy and Department of Electrical Engineering and Computer Science, Vanderbilt University, Nashville, Tennessee 37235, United States of AmericaE-mail: [lhbao@iphy.ac.cn](mailto:lhbao@iphy.ac.cn) and [xlin@ucas.ac.cn](mailto:xlin@ucas.ac.cn)**Keywords:** graphene, degradation, imperfections, four-probe measurements, electrical propertiesSupplementary material for this article is available [online](#)**Abstract**

In large-scale electronic applications of graphene, imperfections play a key role in controlling the electrical properties. Here we directly probe the electrical-degradation effects induced by wrinkles, grain boundaries, multilayered islands, cracks, holes, and adsorbates on millimeter-scale graphene on a SiO<sub>2</sub>/Si substrate using a four-probe scanning tunneling microscope. By comparing the local measurements near and far away from these imperfections, we quantify their impact on the most important figures of merit including sheet resistance, carrier mobility, and residual carrier-density variations in the vicinity of the imperfections. Angle-dependent measurements via a van der Pauw geometry are then performed to determine the influence of imperfections on the whole graphene flake. A key result is that, as long as the imperfections do not extend continuously over the entire flake, the overall electrical properties of a graphene flake are not distinctly impacted by the imperfections because carriers find the paths of least resistance. The four-probe method can also be extended to evaluate the degradation effects on electrical-transport properties in other two-dimensional (2D) materials.

**Introduction**

Graphene, the first-discovered two-dimensional (2D) material [1], is extensively investigated for applications in field-effect transistors, optoelectronic devices, and flexible and transparent electrodes due to its high carrier mobility, exceptional optoelectronic properties, optical transparency, and flexibility [2–4]. Inspired by these and other promising applications, large-area macroscopic graphene has been synthesized by numerous techniques [5]. One of the most effective methods to synthesize large-area graphene is chemical vapor deposition (CVD) on metal-foil substrates such as Cu and Ni [2, 6]. Due to imperfections and impurities in the polycrystalline Cu substrate that provide nucleation centers for growth [7], the synthesized graphene is usually polycrystalline,

whereby the one-dimensional (1D) grain boundaries (GBs) scatter charge carriers and decrease carrier mobility [8, 9]. In addition, multilayer graphene islands can also form between the top layer and the Cu substrate with an inverse 'step pyramid' stacking structure [10, 11].

After graphene is grown on a conducting substrate, it must be transferred to an insulating substrate for electrical characterization and device integration. During the post-growth transfer process, surface adsorbates, microns-wide wrinkles, extended cracks, and irregular holes are introduced. All these imperfections, namely wrinkles, GBs, multilayer islands, cracks, holes, and adsorbates, reduce graphene's homogeneity and result in additional carrier scattering during electrical transport, degrading the electrical performance and limiting practical applications in electronics

[9, 12–15]. A deep understanding of the electrical degradation effects induced by graphene imperfections is highly needed.

Experimental studies of degradation effects induced independently by graphene wrinkles [16], GBs [17, 18], multilayered islands [19, 20], adsorbates [15, 21], and cracks and holes [22, 23] have been performed by conventional two- and four-terminal measurements, which entails lithographically patterning the graphene films into electrical devices with drain and source electrodes [16, 17, 20]. The micro-fabrication process inevitably introduces additional contamination, irreversibly damages the sample, and changes the intrinsic electrical properties [12]. In contrast, four-probe electrical measurements performed by an ultra-high-vacuum (UHV), four-probe, scanning-tunneling-microscopy (4P-STM) system can avoid additional contamination and preserve the original quality and intrinsic properties of the samples after characterization [24–26]. Moreover, the 4P-STM system can measure samples with any geometrical shape by placing probes at various positions and length scales, exploiting the versatility of individually-driven probes with nm resolution [27]. Therefore, the 4P-STM is an effective way to systemically study electrical properties of large-scale graphene with a wide assortment of imperfections.

Here we report direct probing of the effect of imperfections on the electrical properties of millimeter-scale graphene, typically of samples 1 mm in size, including sheet resistance ( $R_{\square}$ ), carrier mobility ( $\mu$ ), and residual carrier-density ( $n_0$ ) variations, by a 4P-STM system. By performing local four-probe measurements, it is found that imperfections lead to a local increase of the sheet resistance  $R_{\square}$  by up to 650% while the mobility  $\mu$  decreases by up to 95%. Both global van der Pauw measurements and local four-point measurements in regions far away from imperfections reveal that imperfections have no distinct effect on the electrical homogeneity of the whole graphene flake unless they are quite extended, as can be the case with multilayered islands and cracks. Overall, the whole graphene flake shows better electrical performance than local regions with imperfections. The present method can be extended to characterize the electrical properties of other 2D materials.

## Results and discussion

The graphene samples were grown on Cu foil by the CVD method and then transferred onto a SiO<sub>2</sub>/Si substrate [28]. The polycrystalline graphene flakes with irregular shapes can be easily identified on Cu foil after growth, as shown in the optical image in figure 1(a). The growth process of graphene is not encumbered by GBs or the morphology of the Cu substrate, leading to grains of millimeter size or larger [28]. Figure 1(b) shows one of the typical STM images of graphene on Cu foil, revealing the

highly-corrugated nature of the substrate. The presence of both triangular and honeycomb lattices in the atomic-resolution STM image (figure 1(c)) is attributed to the local corrugations of the Cu surface, which cause anisotropic strain effects, leading to breaking the six-fold symmetry of the graphene carbon lattices [29]. An optical micrograph of graphene transferred onto a SiO<sub>2</sub>/Si substrate is shown in figure 1(d), wherein wrinkles, GBs, multilayered islands, cracks, holes, and adsorbates are indicated by blue, green, red, purple, yellow and black arrows, respectively. In addition to the optical contrast, the thickness obtained by the AFM height image ( $\sim 1.2$  nm) also verifies the monolayer nature of the transferred graphene flakes [30], as shown in figure 1(e). Using two STM probes, we performed STM imaging of graphene on a SiO<sub>2</sub>/Si substrate. As shown in figure 1(f), the triangular and honeycomb atomic structures are clearly resolved for graphene transferred to the SiO<sub>2</sub>/Si substrate.

The electrical properties of the transferred graphene samples were characterized by a home-designed UHV 4P-STM system (see methods) [25]. In the four-probe electrical experiments, probe 1 injects the current ( $I_1$ ), probe 4 is grounded ( $G_4$ ), while probes 2 and 3 measure the potential drop  $V_{23}$  ( $V_2-V_3$ ) between them. In general, the four probes are usually arranged in square, collinear or van der Pauw geometry setups. The sheet resistances  $R_{\square}$  are obtained after multiplying measured  $R_{I_1V_{23}}$  ( $V_{23}/I_1$ ) by certain geometry factors, which are determined according to the probe spacing or the ratio between two measurements (see details in supplementary material ([stacks.iop.org/TDM/6/045033/mmedia](http://stacks.iop.org/TDM/6/045033/mmedia))) [31]. By applying a tunable gate voltage to the heavily-doped Si layer that acts as gate electrode, the carrier densities of graphene on the 300 nm SiO<sub>2</sub> dielectric layer can be varied. Based on the gate-tunable sheet resistances  $R_{\square}$ ,  $n_0$  variations and carrier mobility can be extracted (see details in supporting information).

For local four-probe measurements in square configuration, the imperfections are located in the center of the square and the side length is  $\sim 150$   $\mu\text{m}$  (figure 2(a)). After that, the square formed by the probes is moved to a non-defective area  $\sim 450$   $\mu\text{m}$  away from the original imperfection region, as shown schematically in figure 2(b). Since the nm-scaled corrugation puddles are five orders smaller than the measurement square (figure 1(f)), the strain-induced inhomogeneity are averaged out. By comparing the key figures of merit of the two electrical measurements in one cycle, including maximum  $R_{\square}$ ,  $n_0$  variations, hole mobility ( $\mu_h$ ) and electron mobility ( $\mu_e$ ), the degradation effects caused locally by each kind of imperfection can be extracted. Four-probe measurements via a van der Pauw geometry are carried out to obtain the electrical properties of the whole graphene flake, as illustrated in figure 2(c) [32].

Typical gate-tunable sheet resistances  $R_{\square}$  near (black curves) and away (red curves) from local

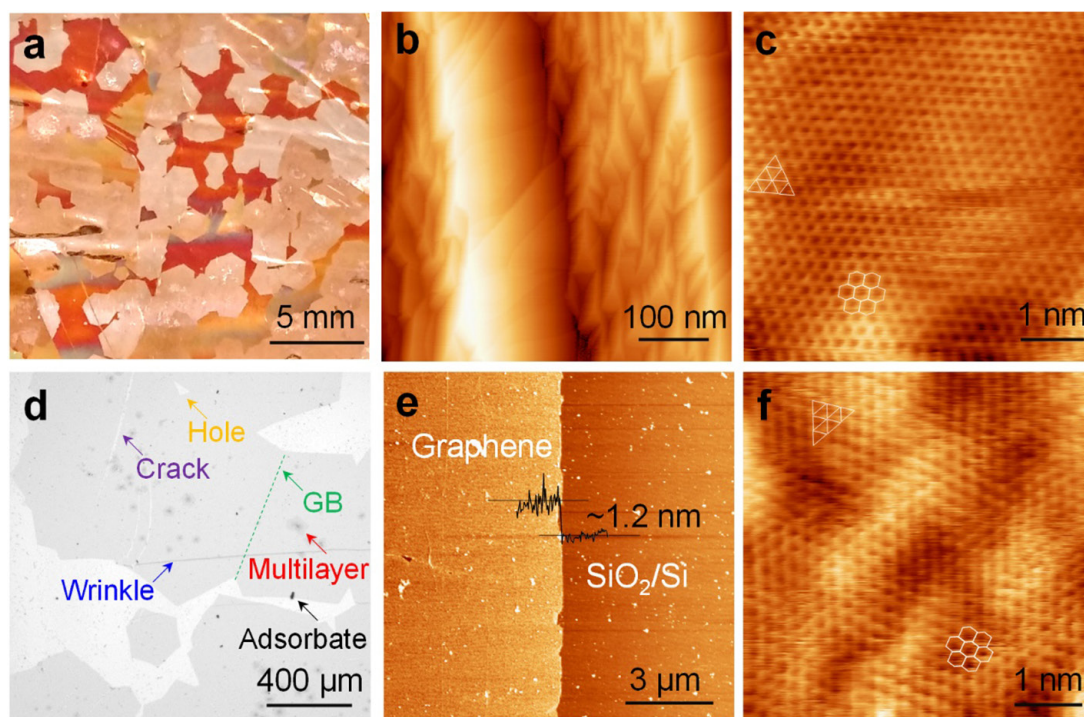


**Figure 1.** Optical, AFM and STM characterization of CVD-grown graphene. (a) Optical micrograph of CVD-grown millimeter-scale graphene flakes on Cu foil. (b) Large-area STM image of graphene on Cu foil. The morphology of the Cu substrate can be clearly resolved. (c) Atomically-resolved STM image of graphene shown in (b). (d) Optical micrograph of transferred graphene on Si/SiO<sub>2</sub> substrate. The selected wrinkles, GBs (highlighted by a green dashed line), multilayered islands, cracks, holes, and adsorbates are indicated by blue, green, red, purple, yellow and black arrows, respectively. (e) AFM height image of the transferred graphene on Si/SiO<sub>2</sub> substrate. The inset line profile reveals that the thickness of the monolayer graphene area is about 1.2 nm. (f) Atomic-resolution STM image of graphene on Si/SiO<sub>2</sub> substrate. The triangular and honeycomb lattices are indicated by triangles and hexagons, respectively. STM imaging parameters:  $I_t = 300$  pA and  $V_{\text{sample}} = -300$  mV.

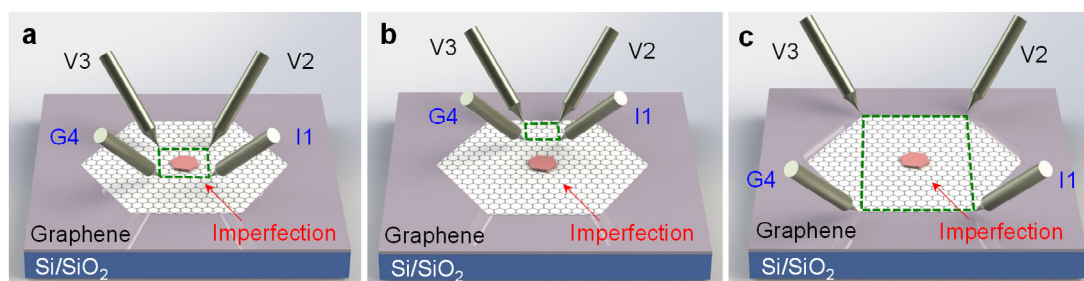


**Figure 2.** Schematic of direct four-probe measurements on graphene via three different configurations. (a) Schematic diagrams of local four-probe measurements with imperfections located in the center of the measurement square. (b) Local four-probe measurement in square configuration directly on monolayer area far away from imperfections. The side length of the square is fixed at  $\sim 150$   $\mu\text{m}$  and the distance between the two configurations in one cycle is  $\sim 450$   $\mu\text{m}$ . (c) Schematic of four-probe measurement by van der Pauw geometry. Probe 1 and 2 contact two nearest corners while probe 3 and 4 contact the corners on the opposite side.

graphene imperfections are shown in figure 3. Except for the multilayered islands, the sheet resistances  $R_{\square}$  near the imperfections are higher than those of regions far away from imperfections in the gate-voltage ( $V_G$ ) range from  $-51$  to  $51$  V. These increases are due to the fact that the local imperfections act as strong scattering centers. As for the multilayered islands, the sheet resistances  $R_{\square}$  in the  $V_G$  range from  $-15$  to  $+15$  V are lower than those in pristine graphene monolayer areas, while at higher  $V_G$  this relationship is reversed. We also performed four-probe collinear measurements across parallel stripe-like multilayered islands, from which

the results show similar trends as the square case (see supplementary figure S1). We will discuss the origin of this behavior shortly.

Based on the four-probe measurements shown in figure 3, the maximum  $R_{\square}$  at the Dirac-point voltage,  $\mu_h$ ,  $\mu_e$ , and  $n_0$  variations are extracted as shown in figure 4. The strong scattering due to the presence of imperfections not only increases the sheet resistance  $R_{\square}$  but also reduces the carrier mobility  $\mu_h$  and  $\mu_e$  by anywhere from 20 to 80%, as shown in figures 4(a)–(c). The similar features of the carrier mobility ratio variations shown in figures 4(b) and (c) indicate that imper-

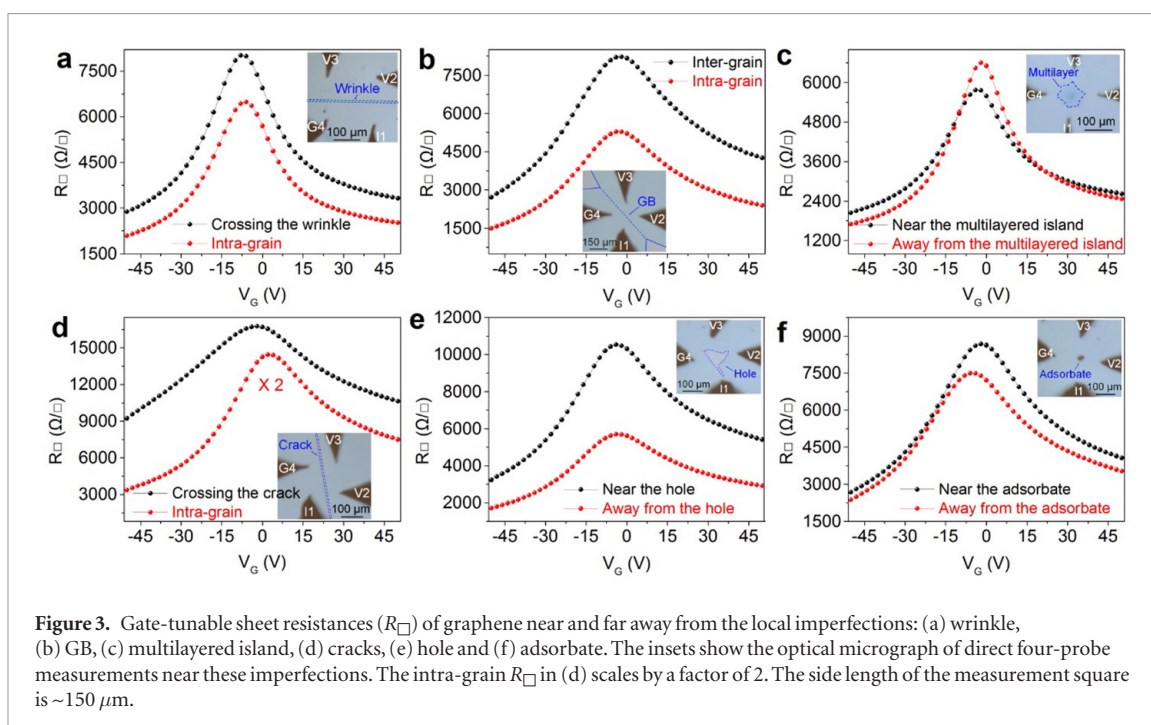


**Figure 3.** Gate-tunable sheet resistances ( $R_{\square}$ ) of graphene near and far away from the local imperfections: (a) wrinkle, (b) GB, (c) multilayered island, (d) cracks, (e) hole and (f) adsorbate. The insets show the optical micrograph of direct four-probe measurements near these imperfections. The intra-grain  $R_{\square}$  in (d) scales by a factor of 2. The side length of the measurement square is  $\sim 150 \mu\text{m}$ .

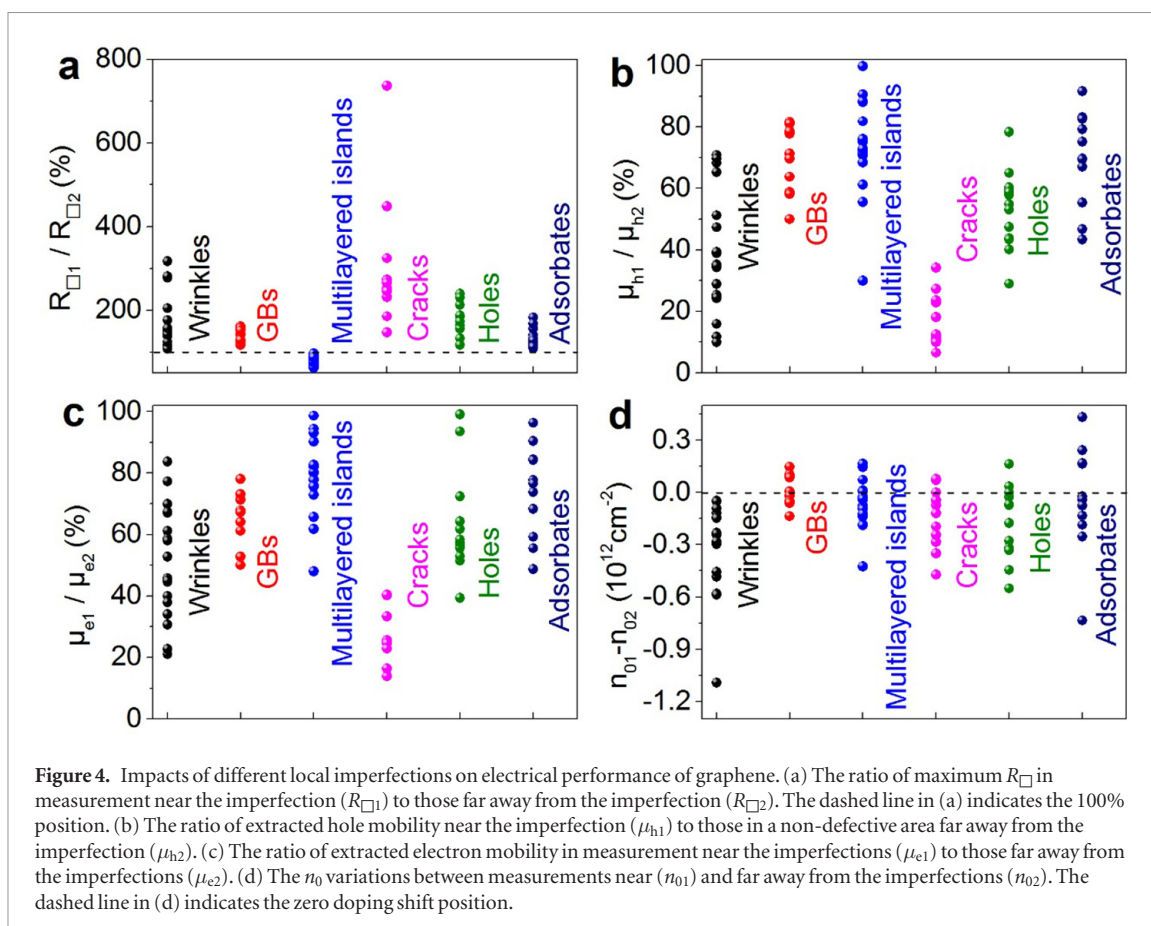


**Figure 4.** Impacts of different local imperfections on electrical performance of graphene. (a) The ratio of maximum  $R_{\square}$  in measurement near the imperfection ( $R_{\square 1}$ ) to those far away from the imperfection ( $R_{\square 2}$ ). The dashed line in (a) indicates the 100% position. (b) The ratio of extracted hole mobility near the imperfection ( $\mu_{h1}$ ) to those in a non-defective area far away from the imperfection ( $\mu_{h2}$ ). (c) The ratio of extracted electron mobility in measurement near the imperfections ( $\mu_{e1}$ ) to those far away from the imperfections ( $\mu_{e2}$ ). (d) The  $n_0$  variations between measurements near ( $n_{01}$ ) and far away from the imperfections ( $n_{02}$ ). The dashed line in (d) indicates the zero doping shift position.

fection-induced degradation has the same effect on both holes and electrons. Compared to other imperfections, the cracks show the largest degradation effects in maximum  $R_{\square}$  ( $\sim$ increased by up to 7.5 times) and  $\mu$  ( $\sim$ decreased by up to 20 times). This feature is due to the fact that the presence of extended cracks leads to discontinuities in conduction channels, where strong short-range scattering potentials are introduced [12, 33].

A hole also causes a discontinuity in the graphene lattice, but the size of typical holes is much smaller than the probe distance, leading to a smaller impact on electrical performance than the impact of cracks. Unlike cracks that break the graphene lattices, wrinkles and GBs are 1D defects formed in the lattice of pristine graphene. The reduction in conductivity and mobility of graphene wrinkles is mainly attributed to scattering of

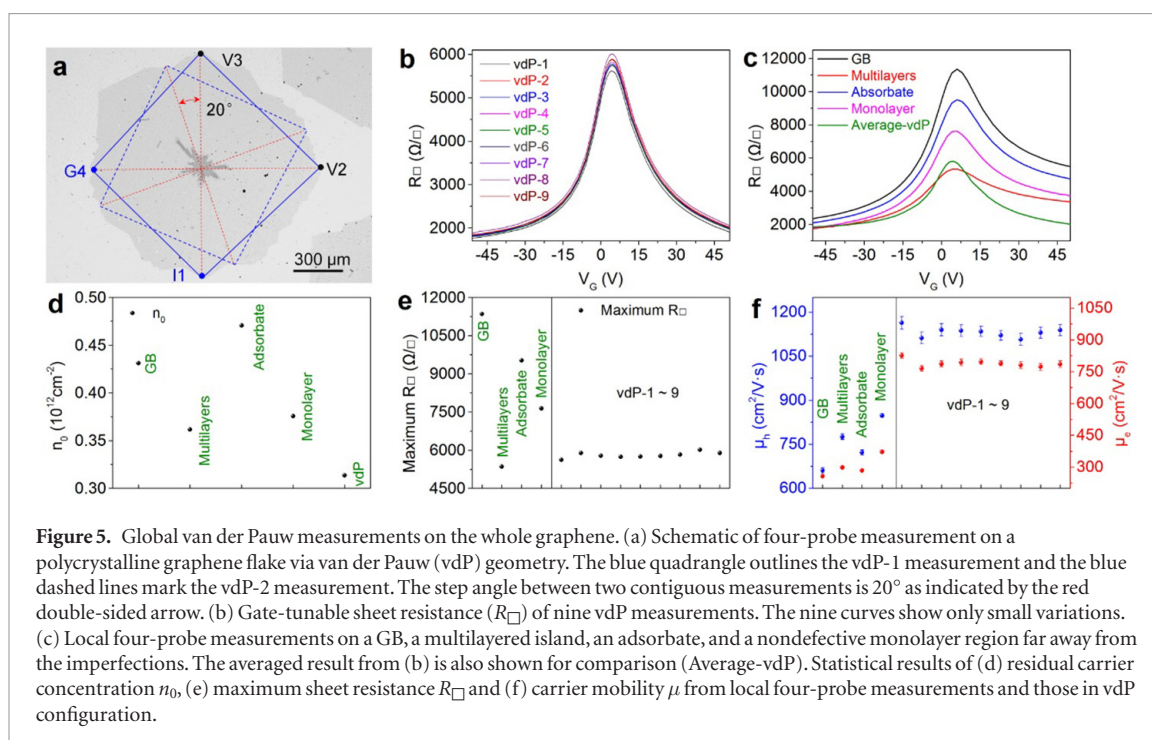
carriers by flexural phonons that stem from the corrugated structures [34], in which curvatures of wrinkle is of vital importance in modifying the electronic band structure [35, 36]. Previous STM studies suggest that the local curvature of the wrinkle can break the six-fold symmetry of the graphene lattice [29, 35]. Through scanning tunneling spectroscopy (STS), lower electrical conductance in wrinkled region was demonstrated compared to relatively flat graphene area due to the presence of midgap states [35]. Moreover, wrinkles can also give rise to n-type doping which forms potential barriers for charge carriers [37, 38]. GBs are composed of non-hexagonal and distorted hexagonal carbon rings [39], in which backscattering and intervalley scattering are the dominant mechanisms responsible for performance degradation [40]. Furthermore, the wider the wrinkle is, the more curved structures are likely present, which can suppress electron transport and mobility [36]. Since the width of graphene wrinkles ( $\sim\mu\text{m}$ ) varies a great deal, the statistical spread of the effect of wrinkles is the greatest. In contrast, the width of GBs is limited to  $\sim 1\text{ nm}$  [39] and thus the statistical spread of their effects is the smallest. As for the adsorbates, the transport properties of graphene near these impurities are dominated by both Coulomb scattering and short-range scattering [15].

As has already been mentioned, the behavior of the sheet resistances  $R_{\square}$  at variable  $V_G$  for multilayered graphene islands is different compared to other imperfections (figures 3(c) and 4(a)). According to previous studies of CVD-grown graphene, these multilayered graphene islands are located beneath the topmost graphene layer with the inverse ‘step pyramid’-type structure [10, 11]. The gradual change of height rather than an abrupt change at the step as demonstrated by the AFM image also verifies the inverse stacking sequence (supplementary figure S2(b)). The lower sheet resistance  $R_{\square}$  near the Dirac-point voltage is mainly attributed to the additional conduction channels provided by the multilayered islands [19]. However, since all the probes contact the topmost graphene layer, the multilayered islands between the dielectric substrate and the topmost layer would cause a screening effect in the gate-tuning process [19, 41]. Therefore, field-induced carriers in the topmost layer are fewer than in the case without screening. As a consequence, at large  $V_G$  bias, the  $R_{\square}$  for the multilayered island area are higher than those in monolayer regions (figure 3(c)). The reduction in carrier mobility  $\mu$  is attributed to two mechanisms (figures 4(b) and (c)). One is the interlayer scattering induced by the multilayered graphene islands [42] and the other is the non-uniformity of the multilayered islands which are composed of both commensurate and incommensurate stacking orders [43, 44], as shown in the Raman maps in supplementary figure S2. The GBs inside the polycrystalline layers give rise to more scattering centers for carriers passing through this area.

The variations of residual carrier-density  $n_0$  between measurements near and far away from the imperfections are shown in figure 4(d). For GBs, multilayered islands, cracks, holes, and adsorbates, both electron- and hole-doping (less than  $1 \times 10^{12}\text{ cm}^{-2}$ ) are present, while for the graphene wrinkles, only electron-doping is observed, which is attributed to electrons transferred from the bulk to the folded regions [37, 38].

To study the effect of imperfections on the electrical properties of the whole graphene flake, global van der Pauw measurements under variable rotation angles are performed, by which the key electrical figures of merit of the whole graphene flakes are extracted. Figure 5(a) shows a schematic diagram of four-probe van der Pauw measurements on a polycrystalline graphene flake with an increment angle of  $20^\circ$ . The GB positions are identified by the Raman D peak mapping as shown in supplementary figure S3 [17]. A multilayered island measuring several hundred micrometers is located in the center with some adsorbates around. For a graphene flake with regular or symmetric shape, e.g. hexagonal graphene shown in figure 2(c), the probes are placed at the corners for the van der Pauw measurements [32]. On the other hand, for a polycrystalline graphene flake with irregular shape shown in figure 5(a), the four contacting points are determined by drawing two orthogonal lines through the center of the flake which intersect with the periphery. Based on this configuration, nine van der Pauw measurements are shown in figure 5(b), in which all curves almost merge with each other and only small variations are present near the Dirac point. The local four-probe measurements inside the same polycrystalline graphene flake and the averaged van der Pauw result are shown in figure 5(c). Figures 5(d)–(f) summarize the residual carrier density  $n_0$  variations, maximum sheet resistance  $R_{\square}$ , and carrier mobility  $\mu$ , respectively. As discussed above, the key electrical figures of merit in the local measurements show large changes. In contrast, the angle-dependent van der Pauw measurements on the whole graphene flake show lower doping, smaller variations, and better electrical performance in terms of sheet resistance  $R_{\square}$  and carrier mobility  $\mu$ . The four-probe measurements on another two polycrystalline flakes with isolated multilayered islands and cross-island wrinkles reveal similar electrical properties as shown in figures S4 and S5 (supplementary material).

Based on these results, we conclude that local imperfections only affect the electrical uniformity in their vicinity but have no distinct impact on the electrical properties of the whole graphene flake. Since the contact points are located at the periphery and nearly equally spaced in the global van der Pauw experiments, the electrons choose paths of least resistance between the two current probes. A similar conclusion regarding paths of least resistance was recently inferred for phonon scattering in semiconductors [45]. Here, the



induced degradation is only effective near the local imperfections, even for the very extended 1D GBs and wrinkles. As a result, the electrical properties of the whole graphene flake are relatively uniform and better than those near the imperfections. Therefore, from the perspective of practical applications, the electrodes can be fabricated at arbitrary positions for graphene-based electrical and optoelectronic devices, such as chemical sensors and photodetectors.

Finally, it should be noted that, if the imperfections are not localized, i.e. their scale is comparable with that of the entire flake, the electrical homogeneity is completely lost. Figure S6(a) (supporting Information) shows four-probe van der Pauw measurements on a polycrystalline graphene flake in which a continuous multilayered region covers  $\sim 1/5$  of the whole flake. The three gate-tunable sheet resistance  $R_{\square}$  curves show considerable differences from each other, indicating a breakdown of the electrical uniformity. Figure S6(b) (supplementary material) shows the global four-probe van der Pauw results on a single-crystal graphene flake with a quite-extended internal crack, the length of which is about  $1/2$  of the side length of the hexagon. Unlike 1D GBs or wrinkles that are embedded in the continuous flake and semitransparent for charge carriers, the cracks entirely disrupt the original conduction channels for the current flows [12]. Thus, the presence of this long crack leads to a breakdown of the electrical uniformity and failure of van der Pauw measurements. The same applies to holes [46].

In summary, we report direct probing of electrical degradation in millimeter-scale graphene on  $\text{SiO}_2$  substrates induced by imperfections, including wrinkles, GBs, multilayered islands, cracks, holes, and adsorbates. Except for the multilayered islands, the presence of imperfections leads to an increase of the local sheet

resistance  $R_{\square}$  by up to 650% while the carrier mobility  $\mu$  decreases by up to 95%. As for multilayered islands, the decrease of  $R_{\square}$  near the Dirac-point voltage is attributed to the additional conduction channels while the reduction of  $\mu$  is mainly due to interlayer scattering and GB-induced scattering. Due to the great variations in width and amount of corresponding curved structures, the electrical figures of merits of graphene wrinkles show the largest spreads. The present results also verify that these local imperfections do not lead to prominent electrical inhomogeneity of the whole graphene flake unless they are quite extended, as can be the case of multilayered islands and cracks. The present study helps pave the way toward practical applications of graphene in electrical and optoelectronic devices and can be used to probe the degradation effects in other 2D materials.

## Methods

The graphene on Cu foil samples were grown by the CVD method [28]. The millimeter-scale graphene flakes were then transferred onto a  $\text{SiO}_2$  (300 nm)/Si substrate by the poly (methyl, methacrylate)-assisted method [28]. Atomic-force-microscopy (AFM) experiments were performed in ambient conditions using a Nanoscope IIIa SPM (Digital Instruments) and all images were acquired in the tapping mode. Raman maps were obtained by a HORIBA HR Evolution Raman microscope system at ambient conditions with 532 nm laser wavelength, a  $0.90/100\times$  objective and  $1\ \mu\text{m}$  beam spot size. The STM imaging experiments and four-probe electrical transport measurements were carried out by a home-designed UHV 4P-STM system with a base pressure at about  $5.0 \times 10^{-10}$  mbar [25]. Before transferred to the

STM chamber, the graphene sheets on Cu foil and on SiO<sub>2</sub>/Si substrates were annealed at 200 °C for 24 h at a pressure of  $\sim 1 \times 10^{-8}$  mbar in the load-lock chamber. The STM images were acquired in constant-current mode using a chemically-etched W tip. All four-probe characterizations were performed with chemically-etched gold tips at room temperature and data were acquired by a Keithley 4200-SCS system. The real-time capacitance signals between the probes and the gate were monitored during the probe approaching process for graphene@SiO<sub>2</sub>/Si [25]. A heavily-doped Si (P<sup>++</sup>/Si) layer acts as gate electrode, by which the carrier densities of graphene on the 300 nm SiO<sub>2</sub> dielectric layer can be tuned.

## Acknowledgments

This work was supported by grants from National Key Research and Development Projects of China (Nos. 2016YFA0202300 and 2018FYA0305800), National Natural Science Foundation of China (Nos. 61674170 and 61888802), the Strategic Priority Research Program of Chinese Academy of Sciences (Nos. XDB30000000, XDB28000000), and Youth Innovation Promotion Association of CAS (20150005). Work at Vanderbilt (STP) was supported by the McMinn Endowment.

## ORCID iDs

Rui-Song Ma  <https://orcid.org/0000-0002-9954-4416>

Jiahao Yan  <https://orcid.org/0000-0002-3333-0669>

Lihong Bao  <https://orcid.org/0000-0002-2942-892X>

Hong-Jun Gao  <https://orcid.org/0000-0002-6766-0623>

## References

- [1] Geim A K and Novoselov K S 2007 The rise of graphene *Nat. Mater.* **6** 183–91
- [2] Bae S et al 2010 Roll-to-roll production of 30-inch graphene films for transparent electrodes *Nat. Nanotechnol.* **5** 574–8
- [3] Bonaccorso F, Sun Z, Hasan T and Ferrari A C 2010 Graphene photonics and optoelectronics *Nat. Photonics* **4** 611–22
- [4] Schwierz F 2010 Graphene transistors *Nat. Nanotechnol.* **5** 487–96
- [5] Lee H C, Liu W-W, Chai S-P, Mohamed A R, Aziz A, Khe C-S, Hidayah N M S and Hashim U 2017 Review of the synthesis, transfer, characterization and growth mechanisms of single and multilayer graphene *RSC Adv.* **7** 15644–93
- [6] Kim K S, Zhao Y, Jang H, Lee S Y, Kim J M, Kim K S, Ahn J-H, Kim P, Choi J-Y and Hong B H 2009 Large-scale pattern growth of graphene films for stretchable transparent electrodes *Nature* **457** 706–10
- [7] Yazyev O V and Chen Y P 2014 Polycrystalline graphene and other two-dimensional materials *Nat. Nanotechnol.* **9** 755–67
- [8] Guo W, Wu B, Li Y, Wang L, Chen J, Chen B, Zhang Z, Peng L, Wang S and Liu Y 2015 Governing rule for dynamic formation of grain boundaries in grown graphene *ACS Nano* **9** 5792–8
- [9] Ma R et al 2017 Direct four-probe measurement of grain-boundary resistivity and mobility in millimeter-sized graphene *Nano Lett.* **17** 5291–6
- [10] Fan L, Wang K, Wei J, Zhong M, Wu D and Zhu H 2014 Correlation between nanoparticle location and graphene nucleation in chemical vapour deposition of graphene *J. Mater. Chem. A* **2** 13123–8
- [11] Robinson J T, Culbertson J, Berg M and Ohta T 2018 Work function variations in twisted graphene layers *Sci. Rep.* **8** 2006
- [12] Peter B, David M A M, Patrick R W, Dirch H P, Jonas Due B, Amaia Z, John G, Ling H and Peter U J 2017 Mapping the electrical properties of large-area graphene *2D Mater.* **4** 042003
- [13] Buron J D et al 2014 Electrically continuous graphene from single crystal copper verified by terahertz conductance spectroscopy and micro four-point probe *Nano Lett.* **14** 6348–55
- [14] Chen J-H, Jang C, Xiao S, Ishigami M and Fuhrer M S 2008 Intrinsic and extrinsic performance limits of graphene devices on SiO<sub>2</sub> *Nat. Nanotechnol.* **3** 206
- [15] Hofmann M, Hsieh Y-P, Chang K-W, Tsai H-G and Chen T-T 2015 Dopant morphology as the factor limiting graphene conductivity *Sci. Rep.* **5** 17393
- [16] Zhu W J, Low T, Perebeinos V, Bol A A, Zhu Y, Yan H G, Tersoff J and Avouris P 2012 Structure and electronic transport in graphene wrinkles *Nano Lett.* **12** 3431–6
- [17] Yu Q et al 2011 Control and characterization of individual grains and grain boundaries in graphene grown by chemical vapour deposition *Nat. Mater.* **10** 443–9
- [18] Clark K W, Zhang X-G, Vlassiok I V, He G W, Feenstra R M and Li A-P 2013 Spatially resolved mapping of electrical conductivity across individual domain (grain) boundaries in graphene *ACS Nano* **7** 7956–66
- [19] Nagashio K, Nishimura T, Kita K and Toriumi A 2010 Systematic investigation of the intrinsic channel properties and contact resistance of monolayer and multilayer graphene field-effect transistor *Japan. J. Appl. Phys.* **49** 051304
- [20] Wu Q, Jung S J, Jang S K, Lee J, Jeon I, Suh H, Kim Y H, Lee Y H, Lee S and Song Y J 2015 Controllable poly-crystalline bilayered and multilayered graphene film growth by reciprocal chemical vapor deposition *Nanoscale* **7** 10357–61
- [21] Wehling T O, Katsnelson M I and Lichtenstein A I 2009 Adsorbates on graphene: impurity states and electron scattering *Chem. Phys. Lett.* **476** 125–34
- [22] Mackenzie D M A et al 2017 Quality assessment of graphene: continuity, uniformity, and accuracy of mobility measurements *Nano Res.* **10** 3596–605
- [23] Nakajima H, Morimoto T, Okigawa Y, Yamada T, Ikuta Y, Kawahara K, Ago H and Okazaki T 2019 Imaging of local structures affecting electrical transport properties of large graphene sheets by lock-in thermography *Sci. Adv.* **5** eaau3407
- [24] Lin X, He X B, Yang T Z, Guo W, Shi D X, Gao H J, Ma D D D, Lee S T, Liu F and Xie X C 2006 Intrinsic current-voltage properties of nanowires with four-probe scanning tunneling microscopy: A conductance transition of ZnO nanowire *Appl. Phys. Lett.* **89** 043103
- [25] Ma R, Huan Q, Wu L, Yan J, Zou Q, Wang A, Bobisch C A, Bao L and Gao H-J 2017 Upgrade of a commercial four-probe scanning tunneling microscopy system *Rev. Sci. Instrum.* **88** 063704
- [26] Nakayama T, Kubo O, Shingaya Y, Higuchi S, Hasegawa T, Jiang C-S, Okuda T, Kuwahara Y, Takami K and Aono M 2012 Development and application of multiple-probe scanning probe microscopes *Adv. Mater.* **24** 1675–92
- [27] Li A-P, Clark K W, Zhang X-G and Baddorf A P 2013 Electron transport at the nanometer-scale spatially revealed by four-probe scanning tunneling microscopy *Adv. Funct. Mater.* **23** 2509–24
- [28] Guo W, Wu B, Wang S and Liu Y 2018 Controlling fundamental fluctuations for reproducible growth of large single-crystal graphene *ACS Nano* **12** 1778–84
- [29] Zhang Y F, Gao T, Gao Y B, Xie S B, Ji Q Q, Yan K, Peng H L and Liu Z F 2011 Defect-like structures of graphene on copper

- foils for strain relief investigated by high-resolution scanning tunneling microscopy *ACS Nano* **5** 4014–22
- [30] Shearer C J, Slattery A D, Stapleton A J, Shapter J G and Gibson C T 2016 Accurate thickness measurement of graphene *Nanotechnology* **27** 125704
- [31] Miccoli I, Edler F, Pfnur H and Tegenkamp C 2015 The 100th anniversary of the four-point probe technique: the role of probe geometries in isotropic and anisotropic systems *J. Phys.: Condens. Matter* **27** 223201
- [32] Ma R-S, Huan Q, Wu L-M, Yan J-H, Zhang Y-Y, Bao L-H, Liu Y-Q, Du S-X and Gao H-J 2017 Direct measurements of conductivity and mobility in millimeter-sized single-crystalline graphene via van der Pauw geometry *Chin. Phys. B* **26** 066801
- [33] Chen J-H, Cullen W G, Jang C, Fuhrer M S and Williams E D 2009 Defect scattering in graphene *Phys. Rev. Lett.* **102** 236805
- [34] Chen W, Gui X, Yang L, Zhu H and Tang Z 2019 Wrinkling of two-dimensional materials: methods, properties and applications *Nanoscale Horiz.* **4** 291–320
- [35] Xu K, Cao P and Heath J R 2009 Scanning tunneling microscopy characterization of the electrical properties of wrinkles in exfoliated graphene monolayers *Nano Lett.* **9** 4446–51
- [36] Deng S and Berry V 2016 Wrinkled, rippled and crumpled graphene: an overview of formation mechanism, electronic properties, and applications *Mater. Today* **19** 197–212
- [37] Ma C, Sun X, Du H, Wang J, Tian M, Zhao A, Yamauchi Y and Wang B 2018 Landau quantization of a narrow doubly-folded wrinkle in monolayer graphene *Nano Lett.* **18** 6710–8
- [38] Kim K et al 2011 Multiply folded graphene *Phys. Rev. B* **83** 245433
- [39] Huang P Y et al 2011 Grains and grain boundaries in single-layer graphene atomic patchwork quilts *Nature* **469** 389–92
- [40] Koepke J C, Wood J D, Estrada D, Ong Z-Y, He K T, Pop E and Lyding J W 2013 Atomic-scale evidence for potential barriers and strong carrier scattering at graphene grain boundaries: a scanning tunneling microscopy study *ACS Nano* **7** 75–86
- [41] Nagashio K, Nishimura T, Kita K and Toriumi A 2009 Mobility variations in mono- and multi-layer graphene films *Appl. Phys. Express* **2** 025003
- [42] Yuanfang Y, Zhenzhen L, Wenhui W, Xitao G, Jie J, Haiyan N and Zhenhua N 2017 Investigation of multilayer domains in large-scale CVD monolayer graphene by optical imaging *J. Semicond.* **38** 033003
- [43] Hwang J-S et al 2012 Imaging layer number and stacking order through formulating Raman fingerprints obtained from hexagonal single crystals of few layer graphene *Nanotechnology* **24** 015702
- [44] Bayle M et al 2015 Dependence of the Raman spectrum characteristics on the number of layers and stacking orientation in few-layer graphene *Phys. Status Solidi b* **252** 2375–9
- [45] Wu Y-N, Zhang X G and Pantelides S T 2016 First-principles calculations reveal controlling principles for carrier mobilities in semiconductors *Semicond. Sci. Technol.* **31** 115016
- [46] Náhlík J, Kašpárková I and Fitl P 2011 Study of quantitative influence of sample defects on measurements of resistivity of thin films using van der Pauw method *Measurement* **44** 1968–79